

Available online at [www.synsint.com](http://www.synsint.com)

# Synthesis and Sintering

ISSN 2564-0186 (Print), ISSN 2564-0194 (Online)



Research article

## Synthesis and sintering of SrTiO<sub>3</sub>–ZnO ceramics: Role of ZnO content on microstructure and dielectric properties



Muhammad Kashif<sup>a</sup>, Muhammad Salman Habib<sup>ID a</sup>, Muhammad Asif Rafiq<sup>ID a,\*</sup>, Moaz Waqar<sup>ID a,b</sup>, Muhammad Asif Hussain<sup>ID c</sup>, Ayesha Iqbal<sup>ID a</sup>, Mehboob Ahmed Abbasi<sup>a</sup>, Shahid Saeed<sup>a</sup>

<sup>a</sup> Department of Metallurgical and Materials Engineering, University of Engineering and Technology, G.T Road, Lahore – 54890, Pakistan

<sup>b</sup> NUS Graduate School for Integrative Sciences and Engineering, National University of Singapore, Singapore 119077, Singapore

<sup>c</sup> Department of Metallurgical and Materials Engineering, University of Punjab Lahore, Pakistan

### ABSTRACT

The classical system of combining modern perovskite and wurtzite structure semiconductor materials is used to model the internal structure for the applications of functional novel electronic devices. The structure-property relation has a significant impact on the properties of metal oxides-based functional ceramics. The structural and electrical properties of SrTiO<sub>3</sub>-xZnO (0 ≤ x ≤ 10 wt%) ceramics produced via solid-state reaction (SSR) were thoroughly examined. X-ray diffraction (XRD) and scanning electron microscopy confirmed the presence of a mono-phase cubic structure with Pm3̄m space group and resulted in increased density respectively. Complex impedance spectroscopy (CIS) was carried out from 300 to 500 °C temperature within the frequency range of 100 Hz to 1 MHz to study the contribution of grain bulk and grain boundary for impedance behavior. Grain boundaries dominated the overall resistance of the samples and the addition of ZnO in SrTiO<sub>3</sub> caused an increase in the overall conductivity. Increasing temperature decreases the resistance of both components, and at higher frequencies that confirms the negative temperature coefficient resistance (NTCR) behavior of the samples. Increasing temperature decreases the relaxation of grain bulk and grain boundary thus predicting the hopping conduction mechanism. The results will be helpful to engineer the microstructure of SrTiO<sub>3</sub> based on practical applications such as sensors, actuators, and energy devices.

© 2023 The Authors. Published by Synsint Research Group.

### KEYWORDS

Semiconductor  
Complex impedance spectroscopy  
Relaxation time  
Hopping conduction  
Sensors



### 1. Introduction

Increasing global demand for energy and the deleterious environmental effects of current energy conversion technologies have urged the research community to develop alternative and sustainable energy conversion systems. Heat dissipated from industrial processes, melting furnaces, power plants, exhaust engine systems, etc., is a low-cost, sustainable, and untapped source of energy [1, 2]. Energy (ED) devices

are capable of converting this waste heat into a useful form of energy such as electricity without any harmful emissions compared to conventional electricity generators being operated on fossil fuels [3]. Thermoelectric devices are also working long-lasting, have low operational cost, with no moving parts, and have good reliability which makes these devices a suitable candidate for heat energy conversion. Until now, thermoelectric, energy generation, and functional devices have been fabricated by using heavy metallic alloys of Pb and Te such

\* Corresponding author. E-mail address: [asifrafiq@uet.edu.pk](mailto:asifrafiq@uet.edu.pk) (M. Asif Rafiq)

Received 18 January 2023; Received in revised form 24 February 2023; Accepted 27 February 2023.

Peer review under responsibility of Synsint Research Group. This is an open access article under the CC BY license (<https://creativecommons.org/licenses/by/4.0/>).  
<https://doi.org/10.53063/synsint.2023.31138>

as PbTe and Bi<sub>2</sub>Te<sub>3</sub> which have high conversion efficiency, but they are toxic in nature and create a huge threat to the environment as well as human health. Additionally, these alloys contain naturally rare elements; hence, their applications are limited to deep structural exploration systems. To overcome these challenges, it is imperative to explore alternative material systems with high energy efficiency. Currently, metal oxides are best suited for alternative thermoelectric materials and hence are the focus of this research effort [4].

The lower the thermal conductivity, the higher the performance of the device. For high-temperature applications, metal oxides are considered interesting candidates due to their lack of toxicity, stability, and low cost. Besides, doping by suitable elements can be employed to improve the Seebeck coefficient, dielectric properties, high-temperature stability, and electrical conductivity of these oxides in comparison to traditional energy devices. However, strong bonding between anions and cations in oxides leads to higher thermal conductivity.

Of all the oxides, SrTiO<sub>3</sub> has been researched extensively due to its versatile properties and application such as an anode for fuel cells [5, 6], in hydrolyzing water for photocatalysis [7, 8], as an oxygen sensor [9], as a substrate for the growth of YBCO superconductor [10], and in thermoelectric devices [11–14]. SrTiO<sub>3</sub> is also used in super-lenses to reveal fine structural detail of materials [15] whereas SrTiO<sub>3</sub> nanotubes have been implemented in orthopedic drug administration [16]. SrTiO<sub>3</sub> is also being used extensively in the microelectronic industry as a varistor [17], and capacitor [18, 19], and these components have been successfully implemented in computers as resistive random access memories (RRAMs) [20]. SrTiO<sub>3</sub> has very useful electrical properties such as wide bandgap (e<sub>g</sub> ~3.22 eV) [21, 22] with n-type nature [23]. The electrical conductivity of SrTiO<sub>3</sub> strongly depends on the number of oxygen vacancies with the oxygen amount in the environment and its partial pressure that can be converted into a p-type semiconductor [9, 24, 25]. In SrTiO<sub>3</sub>, Sr has an oxidation state of +2 [26], whereas Ti and O carry valence of +4 and -2 respectively.

ZnO has been extensively used as a sintering aid to improve the microstructural characteristics of ceramics. Apart from densification, it also affects the dielectric properties and conductivity of metal oxides. However, in-depth electrical characterization of ZnO-doped SrTiO<sub>3</sub> has rarely been done. Complex impedance spectroscopy (CIS) is a crucial technique to characterize the contribution of different microstructural characteristics such as grains, grains boundaries, and point defects to the dielectric properties and conductivity of polycrystalline ceramics. CIS was employed in this work to study the relaxation mechanisms and

conductivity behavior of ZnO-doped SrTiO<sub>3</sub> ceramics at various frequencies and temperatures as given in Table 1.

Hence this work aims to initiate a relationship to develop the microstructure and predict the electrical properties of SrTiO<sub>3</sub> undoped as well as ZnO-doped SrTiO<sub>3</sub> (ST-ZnO) polycrystalline ceramics. Using CIS, we obtained resistance, energy to activate charges, the time required to relax individual grain as well as the grains boundary and its relation to the structure of the ST-ZnO and employing diffraction (XRD) and microscopic techniques (SEM). We further characterized the relaxation mechanisms and underlying defects in the samples using high-temperature impedance analysis. The insight obtained in this work should help design the microstructure of SrTiO<sub>3</sub> based on grain and grain boundary to optimize their electrical properties for various desired applications.

## 2. Experiments

### 2.1. Materials

High-purity chemicals SrCO<sub>3</sub> (Riedel-deHaen 99.9%), TiO<sub>2</sub> (UniChem 99%), & ZnO (DUKSAN 99.9%) precursors in purity mentioned were used for the synthesis of variants of SrTiO<sub>3</sub>-xZnO ceramics.

### 2.2. Preparation rout

Solid-state synthesis for mixed oxide was selected to produce SrTiO<sub>3</sub>-xZnO (ST-xZnO) ceramics where (0 ≤ x ≤ 10 wt%). High-purity powders of starting precursors were weighed in stoichiometric amounts and mixed using a planetary ball mill with zirconia balls for 4 h in ethanol as solvent. The powders obtained from ball milling were dried at 120 °C. The powders were calcined at 1200 °C for 4 h in an inert atmosphere in a box furnace. ZnO was added to the calcined powders with stoichiometric ratios and was again milled for 5 h in a planetary ball mill with the same parameters. Uniaxial pressing was carried out to make pellets for characterization, by using a load of 62 MPa for 60 s over a die with 10 mm diameter. Sintering of pellets was then carried out at 1300 °C in the box furnace for 5 h. After sintering, the structure was verified by using an x-ray diffractometer (XRD) (Model: JEOL JDX-99C) with CuKα (λ=1.5405 Å) and 2θ within the limit of 20–80 ° at scanning angle of 0.02 ° per 3 s. Lattice parameters were obtained by using Jade 5.0 (Materials Data Inc.). Microstructural changes were observed using a scanning electron microscope (SEM) (Model: Nova Nano 450). Impedance spectroscopy was performed by applying silver paint at both faces after polishing and baking at elevated temperature to make a metal-insulator-metal configuration for capacitive and resistive measurements from 100 Hz–1 MHz frequency using a digital LCR meter (Model: LCR TH2829C).

**Table 1.** Processing conditions and dielectric constant for SrTiO<sub>3</sub>.

Processing	Sintering temperature & time	Dielectric constant (1 kHz)	Ref.
SrTiO <sub>3</sub> by sol-gel combustion method	1200 °C/4h	504	[27]
SrTiO <sub>3</sub> with titanyl acylate precursor (pure SrTiO <sub>3</sub> )	1300 °C/4h	320–1062	[28]
Nb <sub>2</sub> O <sub>5</sub> -doped SrTiO <sub>3</sub> by alcohol dehydration process	1450 °C/5h	8000	[29]
SrTiO <sub>3</sub> -xZnO (0%, 5%, 7%, and 10%) (solid state route)	1300 °C/4h	3800–7800	Current work

**Table 2.** Calculated lattice parameter & unit cell volume using Jade 5.0.

Composition	Lattice parameter a (Å)	Unit cell volume a <sup>3</sup> (Å <sup>3</sup> )
SrTiO <sub>3</sub> (ST)	3.884	58.596
ST, 5.0 wt% ZnO	3.896	59.150
ST, 7.0 wt% ZnO	3.898	59.264
ST, 10.0 wt% ZnO	3.900	59.341

### 3. Results and discussion

#### 3.1. XRD characterization of doped and undoped SrTiO<sub>3</sub>

The X-ray interaction with SrTiO<sub>3</sub>-ZnO confirmed the existence of crystalline phases and clarified the addition of ZnO dopant on the crystal structure of SrTiO<sub>3</sub>. Fig. 1a shows the diffraction pattern of ST-xZnO sintered at 1300 °C for 5 hours. All the main peaks were identified according to the powder diffraction for SrTiO<sub>3</sub> (JCPDS No. 73-0661) and the cubic crystal structure was confirmed with space group Pm $\bar{3}$ m (#221) in all the samples. No secondary phases and impurities were found. At the planes (110) diffraction peaks at 32.5 ° for different doping concentrations of ZnO have been compared in Fig. 1b with a straight line drawn. Peak shift (shown by dotted line) towards lower angles, as the amount of ZnO, is increased in SrTiO<sub>3</sub>, shows the increase in lattice parameters of SrTiO<sub>3</sub> which can be attributed to the B-site substitution by Zn as Zn<sup>+2</sup> ions have a relatively bigger size (0.740 Å) as compared to Ti<sup>+4</sup> (0.605Å) [30, 31]. A slight increase in the intensity of diffraction peaks can also be observed with the increase in ZnO, which suggests the improvement of crystallinity possibly due to more effective sintering. The volume of the unit cell and the lattice parameter “a” are presented in Table 2.

#### 3.2. Scanning electron microscopy

The microstructure of sintered samples is observed in Fig. 2 when viewing under a scanning electron microscope (SEM). Fig. 2a represents the morphology of the un-doped SrTiO<sub>3</sub> sample, while Figs. 2b-d represent SEM micrographs of 5%, 7%, and 10.0 wt% ZnO doped ST samples. The pellets were effectively sintered with dense microstructure and the coalescence of grains in doped SrTiO<sub>3</sub> indicates the promotion of liquid phase sintering by the addition of ZnO. There was a slight growth in the grains by when the amount of ZnO was increased. The densification with the decreasing voids and pores was observed in higher concentrations of Zn present which is a fair agreement to those obtained in Co-doped SrTiO<sub>3</sub> [32, 33].

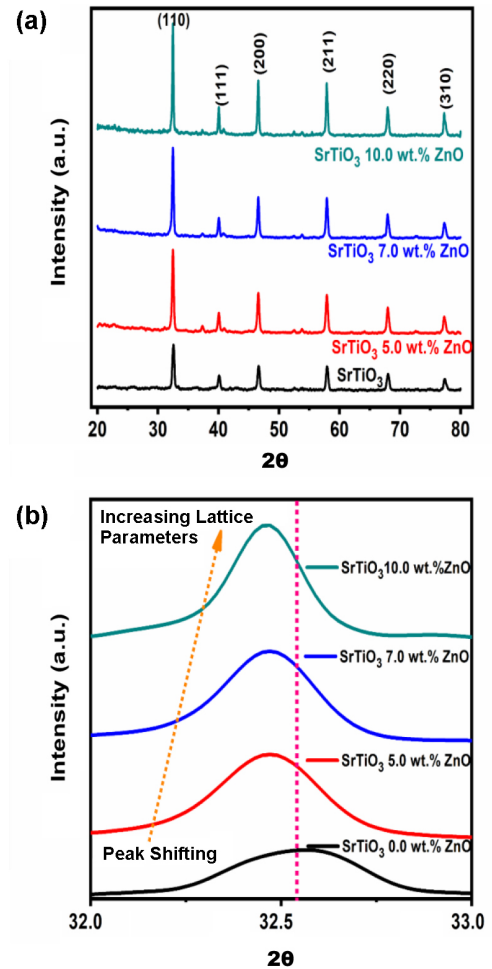


Fig. 1. a) XRD pattern of SrTiO<sub>3</sub>-xZnO (x= 0.0, 5.0, 7.0 & 10 wt%) and b) peak shift towards lower values by the addition of ZnO and it is an indicator of the increased lattice parameter.

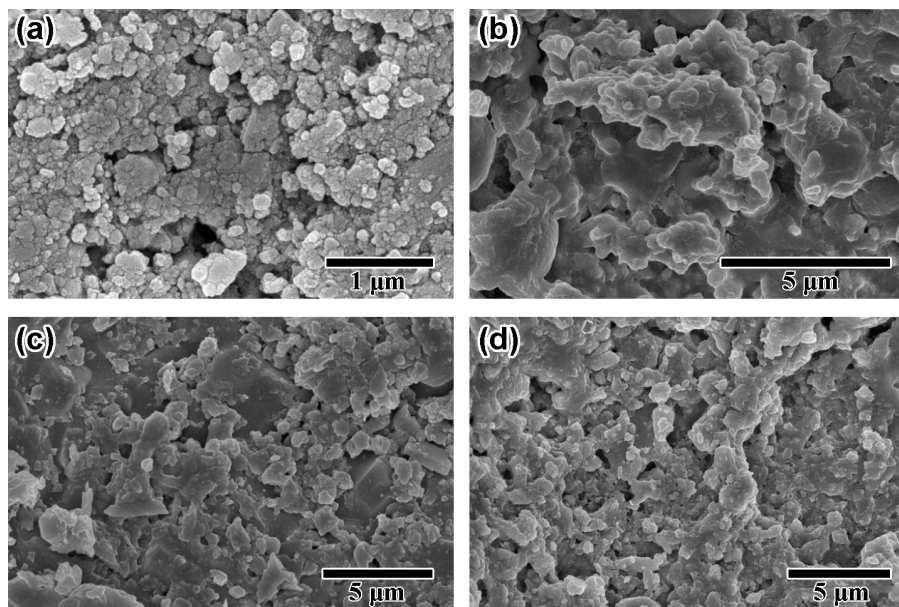
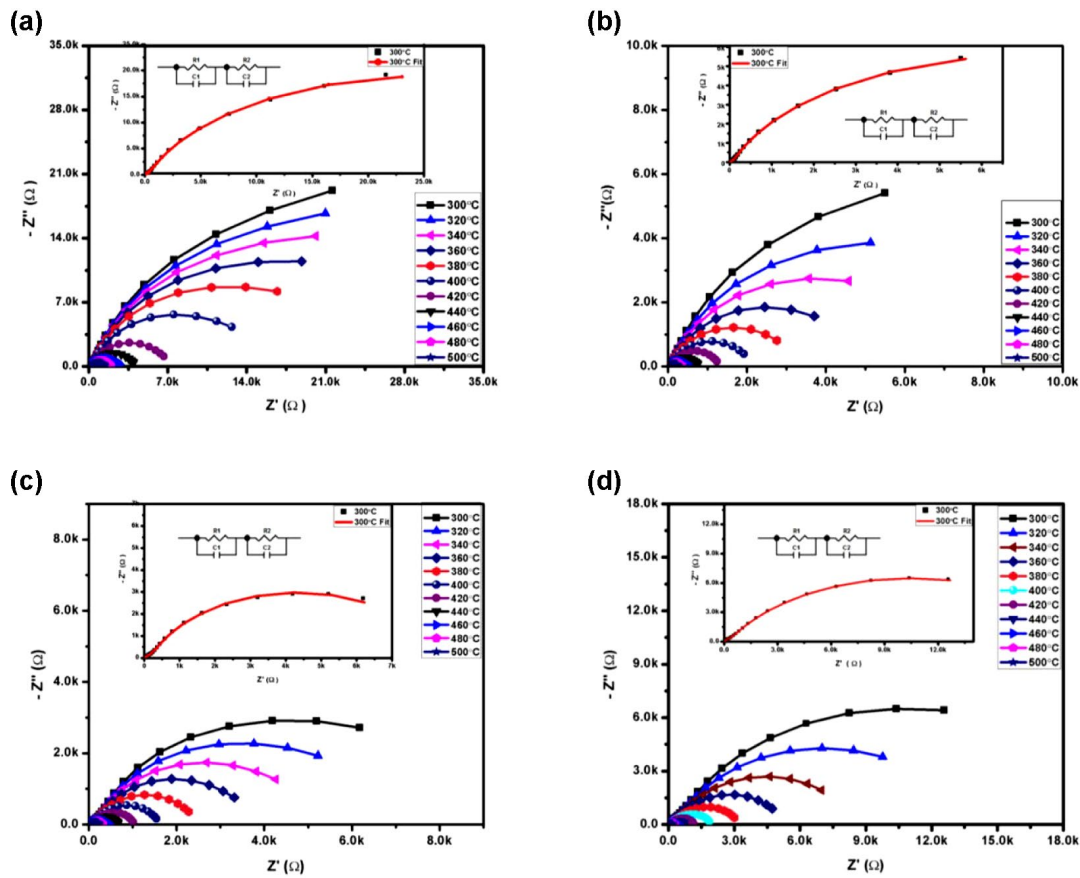


Fig. 2. SEM images showing a) ST-0% ZnO, b) ST-5% ZnO c) ST-7.0% ZnO, and d) 10.0% ZnO.

**Table 3.** Resistance values of ST-ZnO of grain interior and grain boundary at temperatures ranging between 300–500 °C.

Temperature (°C)	SrTiO <sub>3</sub> (ST) 0.0 wt% ZnO		ST- 5.0 wt% ZnO		ST- 7.0 wt% ZnO		ST- 10.0 wt% ZnO	
	R <sub>B</sub> (Ω)	R <sub>GB</sub> (Ω)	R <sub>B</sub> (Ω)	R <sub>GB</sub> (Ω)	R <sub>B</sub> (Ω)	R <sub>GB</sub> (Ω)	R <sub>B</sub> (Ω)	R <sub>GB</sub> (Ω)
300	384.60	28367.00	85.14	7903.00	211.40	5501.00	533.60	11420.00
320	373.90	25483.00	82.52	6020.00	198.80	4458.00	461.00	8187.00
340	361.60	22725.00	79.73	4695.00	183.60	3511.00	387.50	5530.00
360	347.40	19753.00	75.92	3415.00	165.50	2659.00	316.30	3638.00
380	329.90	16082.00	71.45	2381.00	143.20	1792.00	263.10	2258.00
400	308.30	11188.00	66.42	1607.00	122.50	1194.00	203.60	1383.00
420	272.80	5494.00	60.60	1017.00	103.00	768.80	156.00	838.10
440	242.40	3198.00	53.82	596.20	85.91	492.00	118.70	497.30
460	218.40	2161.00	48.73	401.90	71.92	325.70	90.56	293.90
480	196.90	1519.00	43.52	269.80	60.51	224.30	70.90	182.10
500	176.00	1072.00	38.83	189.10	51.23	159.70	57.00	117.50

**Fig. 3.** Cole-Cole plot at 300–500 °C for a) ST-0.0 wt% ZnO, b) ST-5 wt% ZnO, c) ST-7.0 wt% ZnO, and d) 10.0 wt% ZnO. Fitting for 300 °C is shown in the inset.

### 3.3. Electrical characterization

Impedance spectroscopy is used to determine the contribution of various components of the microstructure i.e., the grain interior, grain boundaries, etc. Fig. 3 presents the Cole-Cole plot for all the compositions measured at high temperatures i.e., from 300 to 500 °C starting from the 100 Hz to 1 MHz frequency range. The room temperature data of CIS up to 300 °C is not presented due to the highly insulative nature of samples at lower temperatures. As the temperature goes beyond 300 °C results in a decrease of curvature radius and the semi-circles were found to decrease in the real ( $Z'$ ) axis in all given samples showing the decrease in resistance with an increase in temperature. Two semicircular arcs with different radii were obtained in all the samples which show the contribution from different microstructural regions. For better understanding, an enlarged view is presented as insets in Fig. 3. The first semicircle (at high frequency) with a smaller radius is the representation of bulk (grains) contribution whereas the second semicircle (at low frequency) with a larger radius is the representation of the grain boundaries contribution. This indicates the larger resistance of grain boundaries as compared to the grains which were consistent for all the doped compositions with increasing ZnO presented in Figs. 3b, c & d). Z-view software (V 3.0 Scribner Associates, Inc.) was used to calculate grain boundary resistance ( $R_{GB}$ ) and capacitance ( $C_{GB}$ ) & bulk (grain) resistance and capacitance ( $R_G$ ,  $C_G$ ). The two components connected in series representing grains and grain boundaries form an equivalent circuit in which each consisting of a resistor and a capacitor connected in parallel to each other as also shown in the insets in Fig. 3. Values of resistance and capacitance obtained after fitting are listed in Tables 3 and 4. Here  $R_{GB}$  is the resistance of grain boundary,  $R_G$  is the resistance grain interior offered,  $C_{GB}$  is the capacitance of grain boundary and  $C_G$  is grain interior capacitance. In all cases, fitting was done to verify and explained the experimental value as can be seen in the insets [34, 35]. It can be seen in Table 3 that the resistance of grain boundaries is larger than bulk resistance at all temperatures for all compositions. Additionally, the substitution by Zn results in the decrease of bulk and boundary resistance (grain) of the samples up to 7 wt% which can be accredited for the enhancement in AC conductivity in the samples. However, the resistance increases slightly when the doping concentration similarly approaches 10 wt%, it is evident from Table 4 that the capacitance of grain boundaries is larger than that of bulk for all compositions, and the capacitance of samples increases with the addition of ZnO dopant.

The modulus forms of impedance data are shown in Fig. 4 from 300–500 °C. It can be seen from the graphs that the semicircular arcs of the complex modulus plots predict the behavior of increasing radii of semicircles as the frequency increases. The capacitance values by increasing the amount of ZnO in Strontium Titanate. The contribution of grain is lower than the grain boundaries. Table 4 shows the values of the capacitance of the grain and grain boundary [36].

The center of semicircles in the Cole-Cole plots lies below the real ( $Z'$ ) axis indicating the non-Debye type relaxation mechanism. The relaxation of grain boundaries occurs at low frequency predicting that the time is greater for boundary than that of grain interior. The relaxation behavior can be calculated by using the relation  $\tau = RC$  where  $\tau$ ,  $C$  and  $R$  are the relaxation time, capacitance and resistance, respectively. By using the values of capacitance and resistance from Tables 3 and 4, relaxation times are calculated and presented in Table 5. It is evident from Table 5 that the time of relaxation of both

grain boundary and grain (bulk) interior decreases as temperature increases. Overall, the relaxation times for both grain interior and grain boundary decrease with the addition of ZnO specifically at high temperatures. Fig. 5 shows the Bode plots for real ( $Z'$ ) and imaginary ( $Z''$ ) components of the impedance from 300–500 °C within the range starting from frequency 100 Hz–1 MHz. The increasing temperature increases the AC conductivity ( $\sigma_{ac}$ ) for all the compositions while the increasing frequency decreases the impedance with merging at the single point. This is mainly due to the defects in perovskites such as vacancies present due to oxygen which can move freely at higher temperatures contributing to the increased AC conductivity ( $\sigma_{ac}$ ). The dispersive nature of  $Z'$  at lower frequencies at all the temperatures which merge at higher frequencies indicates that the space charge polarization exists [37, 38]. As the temperatures increase, the frequency and temperature have no effect on the impedance. A similar trend was observed for all the compositions.

Fig. 6 reveals the subordination of the imaginary part of impedance ( $Z''$ ) on the frequency at the temperature range from 300–500 °C. The graphs show that the value of  $Z''$  increases at higher frequencies and reaches a maximum i.e., relaxation peak  $Z''_{max}$  at lower frequencies (between 100 Hz–1 kHz). The relaxation peak moves toward a region where the frequency is higher as the temperature is increased for all the samples as also reported earlier [39–42]. The impedance at a maximum value when reached decreases with an increase in temperature pointing to relaxation behavior. The maximum peak obtained was shifted towards the higher region of the frequency with the rise in temperature which is the clear agreement for faster relaxation [43, 44]. As predicted by the Maxwell Model, the dielectric behavior of material consists of many grains that are active and separated by boundaries that are highly resistive. The applied voltage changes at the grain boundaries producing space charge polarization by creating the poles [45]. Temperature-dependent peak shift at a specific frequency is related to the relaxation in the electrical process in the material which is related to a decrease in relaxation time ( $\tau$ ) [46]. Immobile species are present at lower temperatures and mobile defects are present at higher temperatures. This relaxation phenomenon might be caused by increased electrical conductivity due to the higher mobility of defects. Accumulation of space charges in the material causes the merging of values of  $Z''_{max}$  at lower and higher temperatures [39, 41, 47]. Widening of the peak with the rise in temperature is a good agreement for the space charge polarization which is confirmed. [31]. At lower frequencies, dispersion in curves was observed at different temperatures but it vanished as the frequency increased which might be related to the fact that at higher frequencies (>100 kHz) space charge polarization is less possible [48]. Fig. 7 presents plots in Arrhenius formalism between comparing grain bulk and grain boundary relaxation time versus the reciprocal of temperature for un-doped ST, 5.0 wt% ZnO doped ST, 7.0 wt% ZnO doped ST, and 10.0 wt% ZnO doped ST. A straight line is plotted with the fitting of points when  $1000/T$  plotted against  $\tau$  indicating the presence of thermally activated processes.

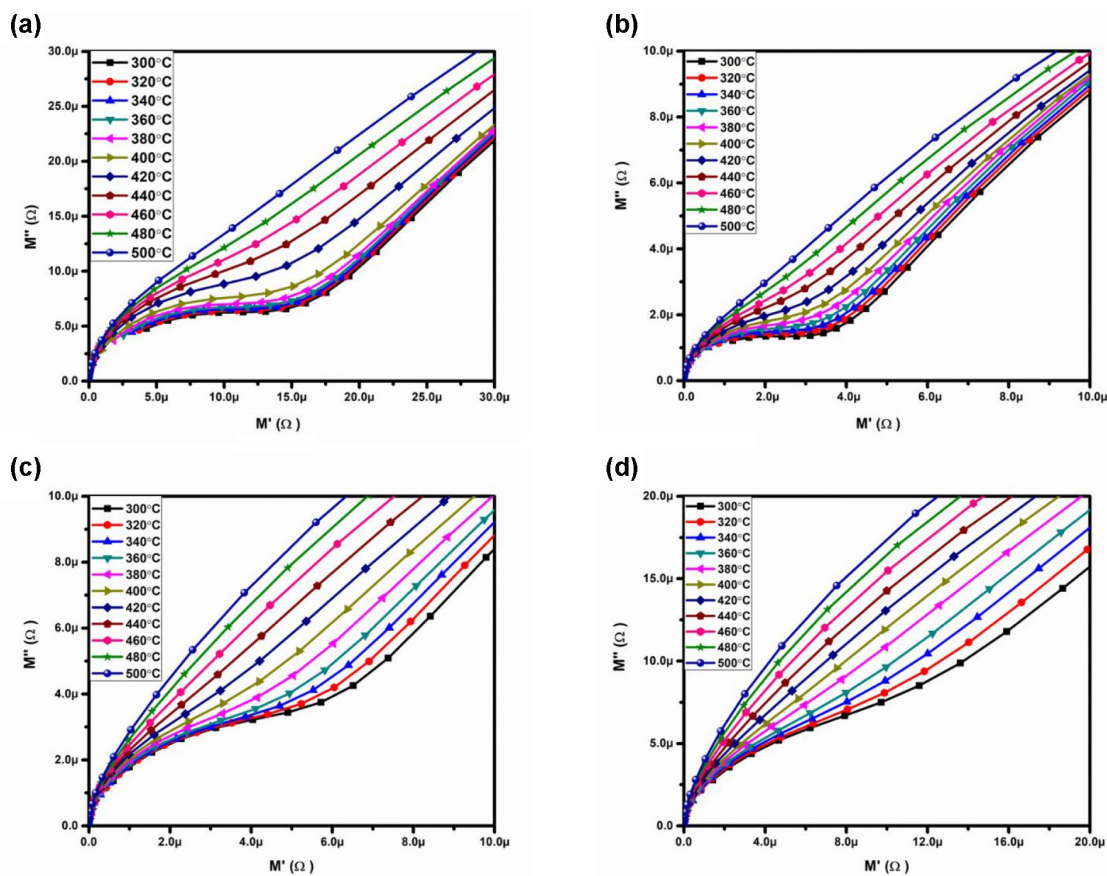
Arrhenius equation is used to calculate the activation energies of grain and grain boundary [49].

$$\tau = \tau_0 \exp(E_a/K_B T) \quad (1)$$

where  $K_B$  is Boltzmann's constant ( $8.6173 \times 10^{-5}$  eV.K<sup>-1</sup>),  $E_a$  is activation energy &  $\tau_0$  is the pre-exponential factor. Activation energies

**Table 4.** Capacitance values of ST-ZnO of grain interior and grain boundary at temperatures ranging between 300–500 °C.

Temperature (°C)	SrTiO <sub>3</sub> (ST) 0.0 wt% ZnO		ST- 5.0 wt% ZnO		ST- 7.0 wt% ZnO		ST- 10.0 wt% ZnO	
	C <sub>B</sub> (nF)	C <sub>GB</sub> (nF)	C <sub>B</sub> (nF)	C <sub>GB</sub> (nF)	C <sub>B</sub> (nF)	C <sub>GB</sub> (nF)	C <sub>B</sub> (nF)	C <sub>GB</sub> (nF)
300	2.78	20.60	9.99	88.44	4.89	50.00	3.14	25.09
320	2.76	20.66	9.95	89.07	4.90	51.34	3.11	26.21
340	2.75	20.64	9.89	89.13	4.93	52.44	3.09	27.18
360	2.75	20.54	9.86	88.88	5.05	53.28	3.11	27.88
380	2.74	20.33	9.90	88.30	5.14	53.53	3.26	28.69
400	2.75	19.90	9.99	87.28	5.28	53.13	3.41	29.31
420	2.74	19.16	10.13	86.15	5.45	52.35	3.61	29.77
440	2.72	18.71	10.29	85.40	5.62	51.54	3.82	30.33
460	2.71	18.49	10.38	85.52	5.73	50.85	3.99	31.60
480	2.70	18.38	10.40	86.22	5.78	50.40	4.10	33.48
500	2.69	18.34	10.34	87.06	5.77	50.07	4.14	36.12

**Fig. 4.**  $M'$  vs.  $M''$  at 300–500 °C for a) ST-0.0 wt% ZnO, b) ST-5 wt% ZnO, c) ST-7.0 wt% ZnO, and d) 10.0 wt% ZnO.

**Table 5.** Relaxation behavior of ST-ZnO of grain interior and grain boundary ranging between 300–500 °C.

Temperature (°C)	SrTiO <sub>3</sub> (ST) 0.0 wt% ZnO		ST- 5.0 wt% ZnO		ST- 7.0 wt% ZnO		ST- 10.0 wt% ZnO	
	$\tau \times 10^{-5}$ (s)							
	$\tau_B$	$\tau_{GB}$	$\tau_B$	$\tau_{GB}$	$\tau_B$	$\tau_{GB}$	$\tau_B$	$\tau_{GB}$
300	0.1067	58.4417	0.0851	69.8902	0.1033	27.5022	0.1674	28.6551
320	0.1033	52.6351	0.0821	53.6201	0.0974	22.8874	0.1434	21.4573
340	0.0996	46.9067	0.0788	41.8475	0.0906	18.4127	0.1197	15.0294
360	0.0954	40.5707	0.0748	30.3532	0.0836	14.1661	0.0982	10.1427
380	0.0905	32.6883	0.0708	21.0252	0.0736	9.5928	0.0858	6.4780
400	0.0848	22.2686	0.0664	14.0253	0.0646	6.3440	0.0693	4.0534
420	0.0747	10.5271	0.0614	8.7610	0.0562	4.0247	0.0563	2.4950
440	0.0659	5.9825	0.0554	5.0913	0.0483	2.5359	0.0453	1.5083
460	0.0591	3.9957	0.0506	3.4372	0.0412	1.6561	0.0362	0.9287
480	0.0531	2.7916	0.0452	2.3262	0.0350	1.1306	0.0291	0.6096
500	0.0473	1.9657	0.0402	1.6464	0.0295	0.7996	0.0236	0.4244

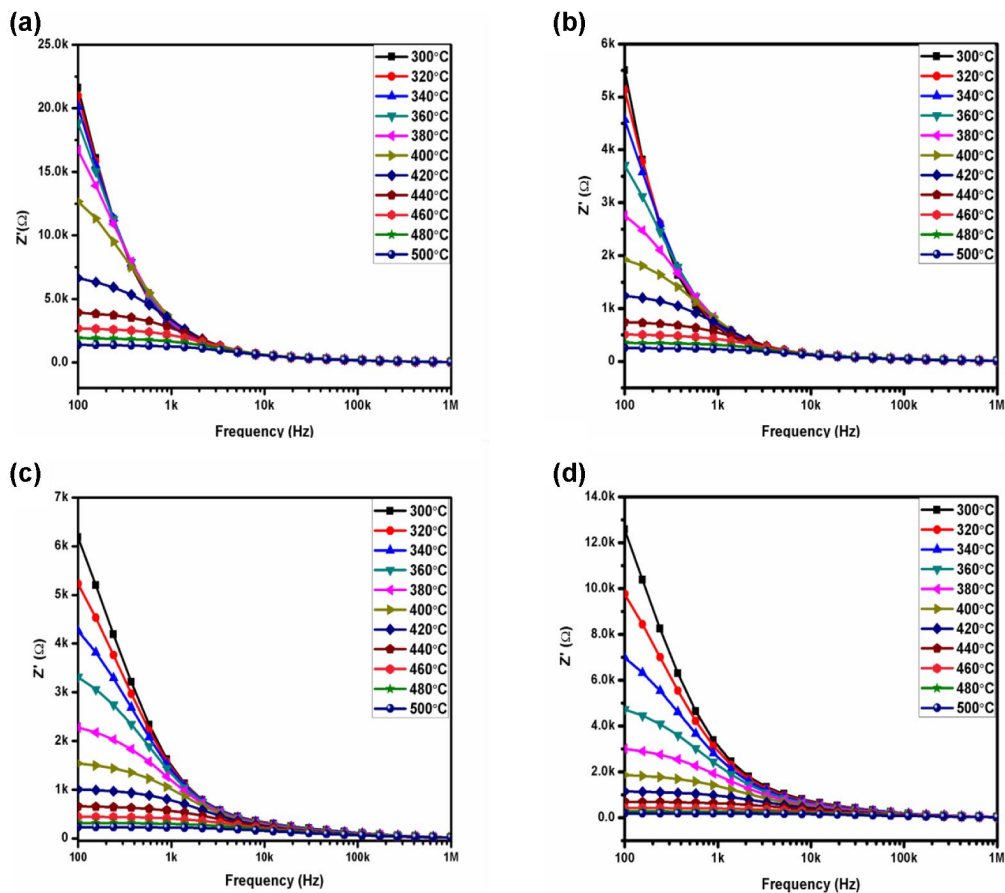


**Fig. 5.** Bode plots for a) un-doped ST, b) 5.0 wt% ZnO doped ST, c) 7.0 wt% ZnO doped ST, and d) 10.0 wt% ZnO doped ST.

**Table 6.** The calculated values of activation energy for grain bulk and interior.

Composition	Activation energy for grain (eV)	Activation energy for grain boundary (eV)
ST-0.0% ZnO	0.07	0.30
ST-5.0 wt% ZnO	0.08	0.53
ST-7.0 wt% ZnO	0.15	0.48
ST-10.0 wt% ZnO	0.29	0.65

for both grain and grain boundary are presented in Table 6 ranging from 0.07 eV to 0.65 eV and the relaxation time is in the range of  $10^{-5}$  s indicating the hopping conduction mechanism [36, 48, 50].

Fig. 8 shows the dielectric loss which is dependent on the temperature at various frequencies (100 Hz–1 MHz) for all the compositions. The loss factor is very important for a dielectric material because this factor represents a loss of energy in dielectrics and depends upon frequency and temperature. Either by increasing temperature or decreasing frequency, the dielectric loss increases for doped and undoped ST. Generally, the behavior of ionic solids is related to both space charge polarization and the conduction process which decreases with

frequency [51, 52]. The loss factor has increased with the addition of ZnO which can be attributed to the increase in the conductivity of samples with the substitution by Zn.

Fig. 9 shows frequency-dependent dielectric constant at different temperatures for un-doped ST, 5.0 wt% ZnO doped ST, 7.0 wt% ZnO doped ST, and 10.0 wt% ZnO doped ST for all the compositions. At higher frequencies, dipoles cannot follow the oscillating field resulting in incomplete polarization which explains that the dielectric of material has decreased with the increase in frequency. At low frequencies, dipoles can steadily reorient and be fully polarized causing an increase in the dielectric constant [53, 54]. The observed higher dielectric constant as the lower frequencies and higher temperatures for all the compositions can also be explained in terms of space charge polarization which almost vanishes at high frequencies while electronic and ionic polarization starts to dominate the overall behavior of the material [54]. Similarly, as the temperature is higher their conductivity increases significantly which can contribute to the increased space charge polarization effect due to enhanced ionic migration at low frequencies. It can also be observed that the dielectric constant of SrTiO<sub>3</sub> increases significantly with the addition of Zn. This can be coordinated as a substitution of tetravalent B-site cation with a divalent ion resulting in the increase in defects such as oxygen vacancies for

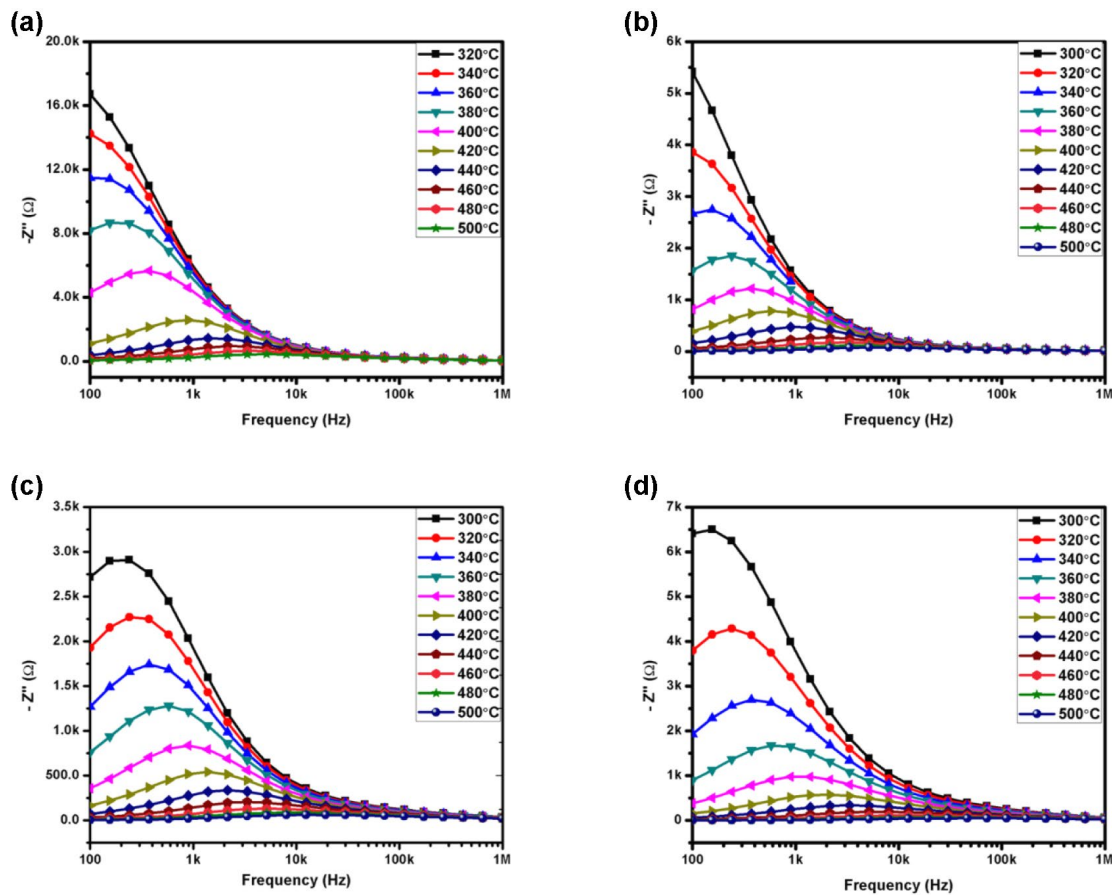


**Fig. 6.** Graphs of the imaginary part of impedance ( $Z''$ ) versus frequency (100 Hz–1 MHz) for a) un-doped ST, b) 5.0 wt% ZnO doped ST, c) 7.0 wt% ZnO doped ST, and d) 10.0 wt% ZnO doped ST.

**Table 7.** Activation energy values calculated at constant frequencies (100 Hz, 1 kHz, and 10 kHz).

Composition	Activation energy (eV)		
	100 Hz	1 kHz	10 kHz
ST- 0.0 wt% ZnO	1.09	0.88	0.36
ST- 5.0 wt% ZnO	0.93	0.77	0.35
ST- 7.0 wt% ZnO	0.85	0.76	0.43
ST- 10.0 wt% ZnO	0.98	0.93	0.65

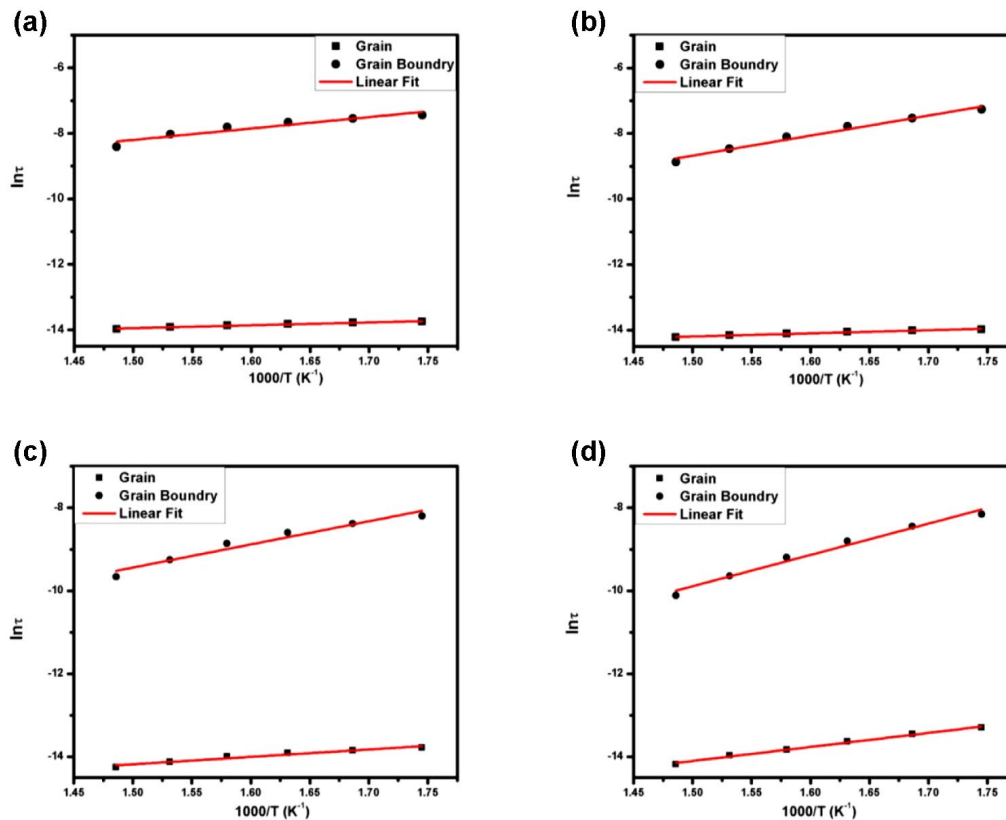
charge compensation. Hence the increase in dielectric constant with the increase in Zn could be due to the increased space charge polarization caused by the higher conductivity and electric polarization. To further characterize the impact of ZnO addition on the conductivity of ST- xZnO, a high-temperature conductivity analysis was performed.

Among Sr and Ca, Sr doped perovskite exhibits superior dielectric behavior for all the temperatures than Ca doped perovskite dielectric ceramics. SrTiO<sub>3</sub> has a dielectric constant of about 300 [55] whereas CaTiO<sub>3</sub> has only 160 [56]. The higher the interfacial polarization of the grain boundary, the higher will be the dielectric constant because of higher resistance & capacitance in comparison to bulk [57]. The dielectric property increases due to the addition of Sr ions present in the SrTiO<sub>3</sub> with that of Ca. Space charge polarization enhances by the smaller charges. All these factors collectively contribute towards a higher dielectric constant in SrTiO<sub>3</sub>.

Fig. 10 presents the variation of  $\ln\sigma_{ac}$  with the reciprocal of temperature (370–475 °C) for all the samples at 1 kHz. The figure clearly shows the increasing temperature with the conductivity increases. To fully establish the conduction mechanism, activation energies were calculated by using the Arrhenius equation [49]. Activation energies calculated for the samples are presented in Table 7.

It is evident that at higher frequencies the activation energy decreases which is mainly due to the inability of charged defects to follow the periodic electric field as discussed earlier. The activation energy of a single ionized oxygen vacancy is usually in the range of 0.3–0.5 eV while it is double for doubly ionized oxygen vacancies i.e., 0.6–1.2 eV [58]. By considering the present scenario, the possible conduction mechanism for the given compositions might be the hope of doubly ionized oxygen vacancies.

Fig. 11 presents frequency-dependent conductivity for all the prepared compositions within the temperature of 300–500 °C. The figure indicates the conductivity climbs exponentially with a linear increase in frequency for all the samples. The addition of ZnO further increases the conductivity of the samples which can be assigned to the increasing vacancies of oxygen concentration. It is evident from Table 7 that the activation energy of oxygen vacancies decreases with the increase in Zn content which is possibly an indication that the concentration of oxygen vacancies increases with an increasing amount of Zn.

**Fig. 7.** Arrhenius fitting plots for AC conductivities ( $\sigma_{ac}$ ) at temperature 300–500 °C a) un-doped ST, b) 5.0 wt% ZnO doped ST, c) 7.0 wt% ZnO doped ST, and d) 10.0 wt% ZnO doped ST.

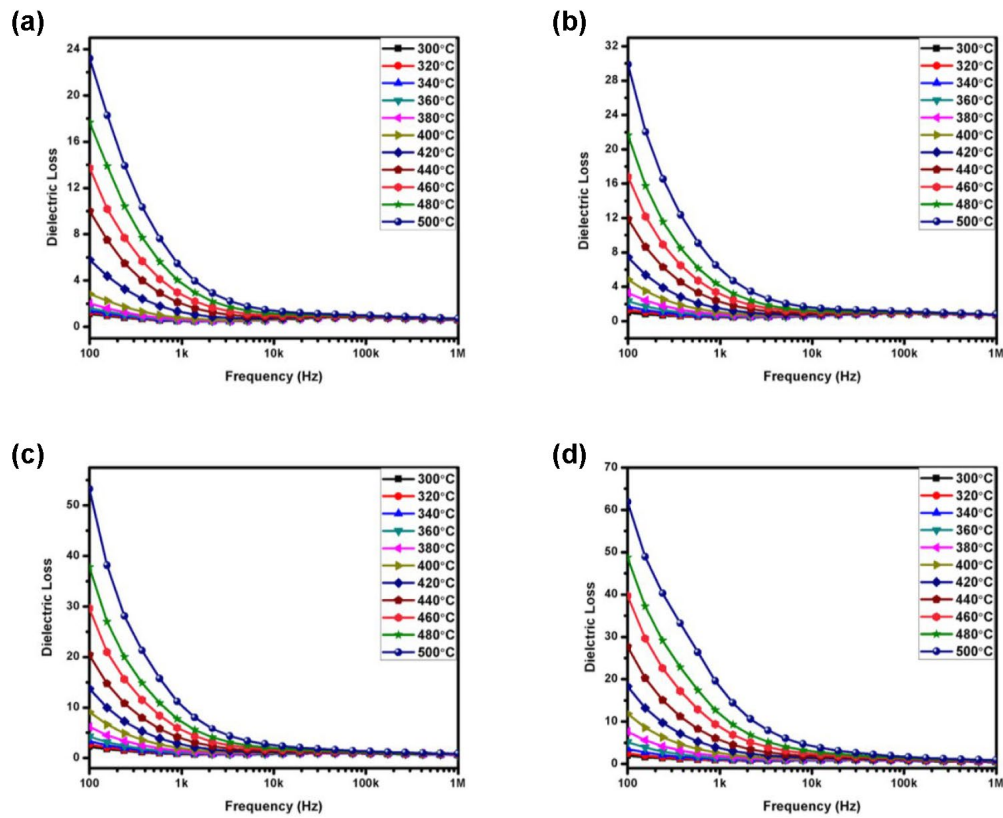


Fig. 8. Frequency dependent dielectric loss of a) un-doped ST, b) 5.0 wt% ZnO doped ST, c) 7.0 wt% ZnO doped ST, and d) 10.0 wt% ZnO doped ST.

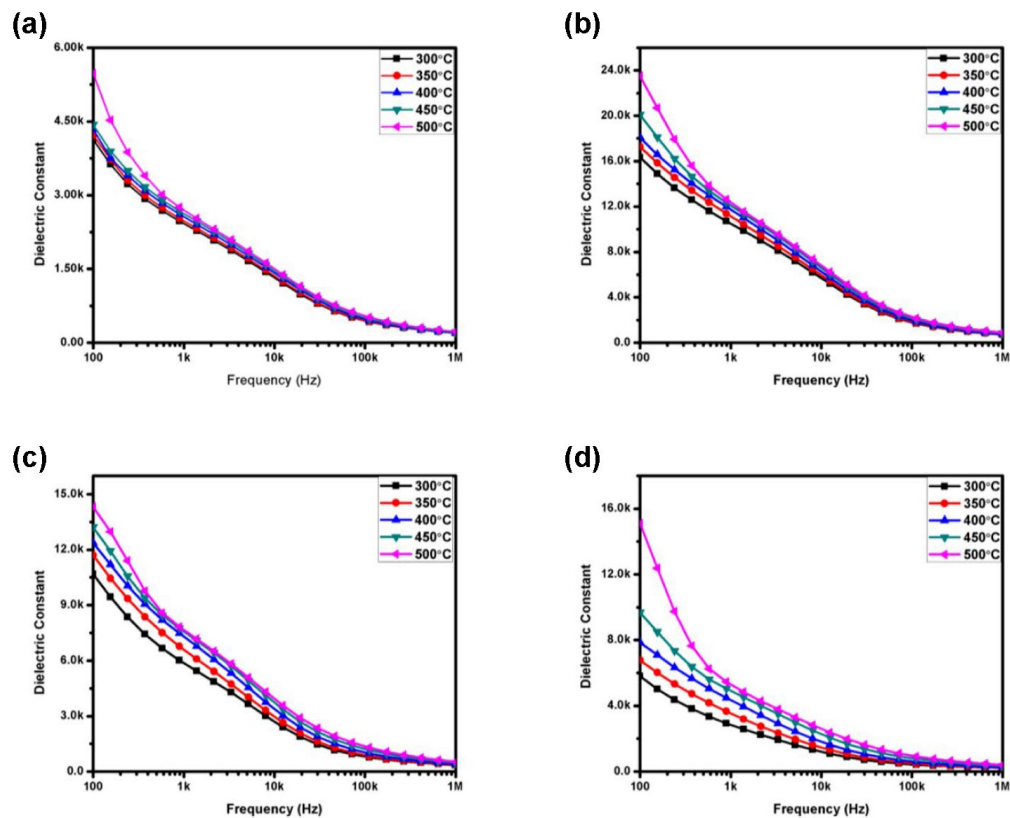


Fig. 9. Dielectric constant with increasing frequency 100 Hz-1 MHz for a) un-doped ST, b) 5.0 wt% ZnO doped ST, c) 7.0 wt% ZnO doped ST, and d) 10.0 wt% ZnO doped ST.

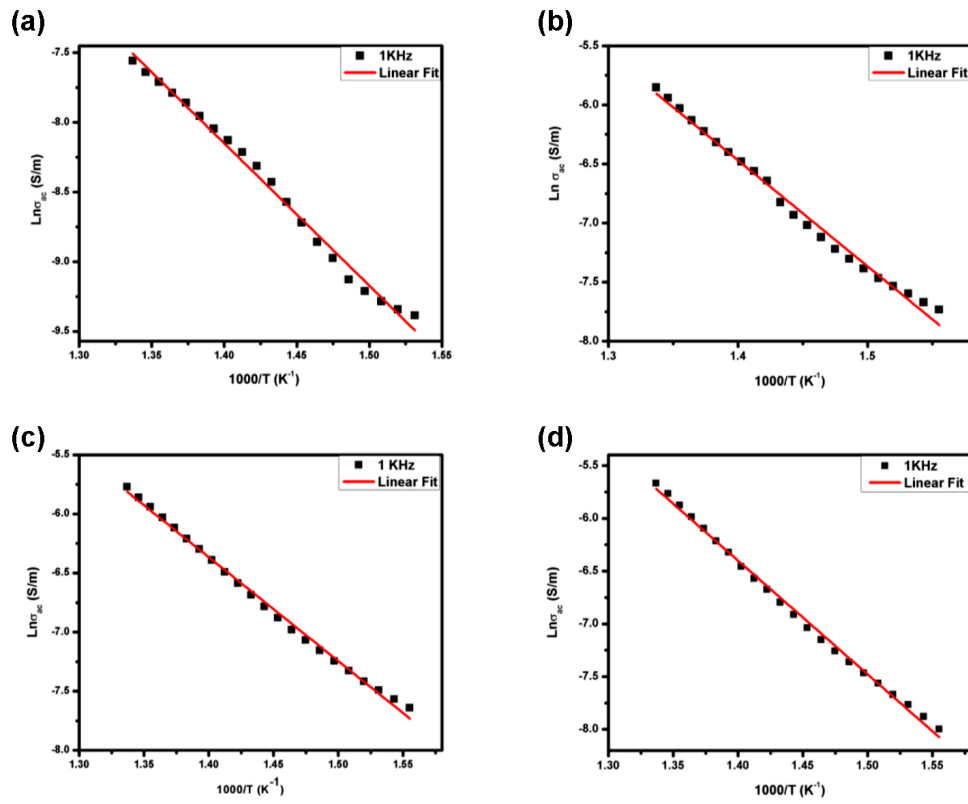


Fig. 10. Graphs representing variation of  $\sigma_{ac}$  versus temperature for a) un-doped ST, b) 5.0 wt% ZnO doped ST, c) 7.0 wt% ZnO doped ST, and d) 10.0 wt% ZnO doped ST.

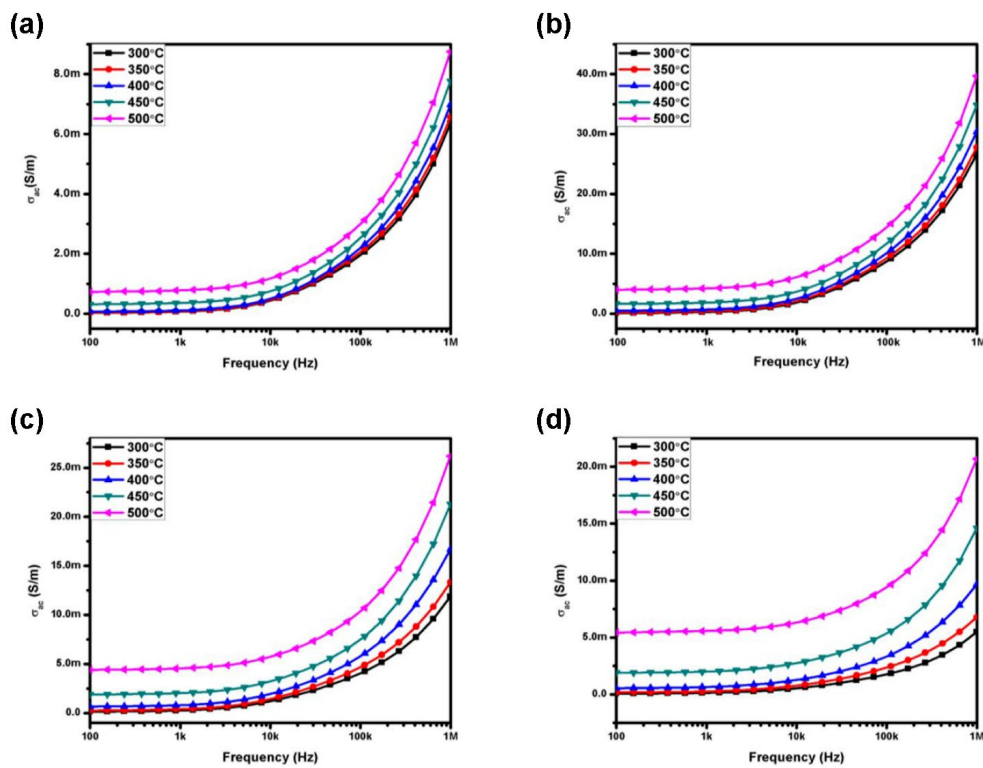


Fig. 11. AC conductivity increases with the addition of Zn attributed by increasing oxygen vacancies with increasing frequency of a) un-doped ST, b) 5.0 wt% ZnO doped ST, c) 7.0 wt% ZnO doped ST, and d) 10.0 wt% ZnO doped ST.

#### 4. Conclusions

The grain and grain boundary contribution by adding ZnO in SrTiO<sub>3</sub> ceramics composites from (0 ≤ x ≤ 10 wt%) analyzed that have been developed via a mixed oxide solid-state reaction. XRD has confirmed the presence of a unique-phase cubic structure with a Pm $\bar{3}$ m space group without any sign of the second phase. Microstructural analysis done with SEM revealed a dense microstructure with ZnO doping. A detailed correlation of electrical properties with the microstructure has been established by using the CIS technique which revealed that the impedance of material has two major contributions i.e., grain bulk and grain boundary. Collectively, the resistance of both grain and grain boundary decreased with rising in temperature indicating higher conductivity at elevated temperatures resulting in a negative temperature coefficient of resistance (NTCR) behavior of the material (an essential requirement for sensors, actuators, and energy devices). The time for the relaxation behavior of both grain bulk and grain boundary has decreased when the temperature increases. This indicates the hopping conduction mechanisms. The dielectric constant of SrTiO<sub>3</sub> ceramics increased greatly with the addition of ZnO. Conduction in ZnO doped SrTiO<sub>3</sub> ceramic was found to be chiefly caused by the hopping conduction of doubly ionized oxygen vacancies as indicated by activation energy values. It was also found that the addition of ZnO might cause an increase in the overall content of oxygen vacancies in the samples. The results obtained in this work will engineer the optimum microstructure of SrTiO<sub>3</sub>-based ceramics composites for improved functionality required for different applications.

#### CRedit authorship contribution statement

**Muhammad Kashif:** Investigation, Writing – original draft.

**Muhammad Salman Habib:** Supervision, Writing – review & editing.

**Muhammad Asif Rafiq:** Resources, Writing – original draft.

**Moaz Waqar:** Conceptualization, Writing – review & editing.

**Muhammad Asif Hussain:** Conceptualization, Methodology.

**Ayesha Iqbal:** Visualization, Writing – original draft.

**Mehboob Ahmed Abbasi:** Investigation, Visualization.

**Shahid Saeed:** Methodology, Resources.

#### Data availability

The authors confirm that data supporting the findings of this study are available within the article and its supplementary material. Raw data that supports the findings of this study are available for the corresponding author, upon reasonable request.

#### Declaration of competing interest

The authors have no conflicts of interest to declare. All co-authors have seen and agree with the contents of the manuscript and there is no financial interest to report.

#### Funding and acknowledgment

The authors express their gratitude to their affiliated universities in Pakistan and Singapore for their invaluable supports, which have been beneficial in conducting this research collaboration.

#### References

- [1] A. Shakouri, Recent developments in semiconductor thermoelectric physics and materials, *Ann. Rev. Mater. Res.* 41 (2011) 399–431. <https://doi.org/10.1146/annurev-matsci-062910-100445>.
- [2] Z. Xiao, K. Kisslinger, E. Dimasi, J.R. Kimbrough, The fabrication of nanoscale Bi<sub>2</sub>Te<sub>3</sub>/Sb<sub>2</sub>Te<sub>3</sub> multilayer thin film-based thermoelectric power chips, *Microelectron. Eng.* 197 (2018) 8–14. <https://doi.org/10.1016/j.mee.2018.05.001>.
- [3] D.K.C. MacDonald, *Thermoelectricity: an introduction to the principles*, Wiley, N.Y. (2006).
- [4] A. Khan, A. Ali, I. Khan, Sintering behavior and microwave dielectric properties of CaTi<sub>1-x</sub>(Nb<sub>1/2</sub>Al<sub>1/2</sub>)<sub>x</sub>O<sub>3</sub>, *Synth. Sinter.* 1 (2021) 197–201. <https://doi.org/10.53063/synsint.2021.1467>.
- [5] Q. Ma, F. Tietz, D. Sebold, D. Stöver, Y-substituted SrTiO<sub>3</sub>-YSZ composites as anode materials for solid oxide fuel cells: Interaction between SYT and YSZ, *J. Power Sources.* 195 (2010) 1920–1925. <https://doi.org/10.1016/j.jpowsour.2009.09.075>.
- [6] S. Ahmadi, Synthesis and characterization of aluminum-yttrium perovskite powder using a co-precipitation technique, *Synth. Sinter.* 2 (2022) 170–175. <https://doi.org/10.53063/synsint.2022.24135>.
- [7] J. Mavroides, J. Kafalas, D. Kolesar, Photoelectrolysis of water in cells with SrTiO<sub>3</sub> anodes, *Appl. Phys. Lett.* 28 (1976) 241–243. <https://doi.org/10.1063/1.88723>.
- [8] F. Wagner, G. Somorjai, Photocatalytic and photoelectrochemical hydrogen production on strontium titanate single crystals, *J. Am. Chem. Soc.* 102 (1980) 5494–5502. <https://doi.org/10.1021/ja00537a013>.
- [9] J. Gerblinger, H. Meixner, Fast oxygen sensors based on sputtered strontium titanate, *Sens. Actuators B: Chem.* 4 (1991) 99–102. [https://doi.org/10.1016/0925-4005\(91\)80183-K](https://doi.org/10.1016/0925-4005(91)80183-K).
- [10] S. Hayward, E. Salje, Cubic-tetragonal phase transition in SrTiO<sub>3</sub> revisited: Landau theory and transition mechanism. *Ph. Transit.* 68 (1999) 501–522. <https://doi.org/10.1080/01411599908224530>.
- [11] H. Obara, A. Yamamoto, C.-H. Lee, K. Kobayashi, A. Matsumoto, R. Funahashi, Thermoelectric properties of Y-doped polycrystalline SrTiO<sub>3</sub>, *Jpn. J. Appl. Phys.* 43 (2004) L540. <https://doi.org/10.1143/JJAP.43.L540>.
- [12] H. Ohta, K. Sugiura, K. Koumoto, Recent progress in oxide thermoelectric materials: p-type Ca<sub>3</sub>Co<sub>4</sub> and n-type SrTiO<sub>3</sub>, *Inorg. Chem.* 47 (2008) 8429–8436. <https://doi.org/10.1021/ic800644x>.
- [13] K. Koumoto, I. Terasaki, R. Funahashi, Complex oxide materials for potential thermoelectric applications, *MRS Bull.* 31 (2006) 206–210. <https://doi.org/10.1557/mrs2006.46>.
- [14] M. Yamamoto, H. Ohta, K. Koumoto, Thermoelectric phase diagram in a CaTiO<sub>3</sub>-SrTiO<sub>3</sub>-BaTiO<sub>3</sub> system, *Appl. Phys. Lett.* 90 (2007) 072101. <https://doi.org/10.1063/1.2475878>.
- [15] S.C. Kehr, Y.M. Liu, L.W. Martin, P. Yu, M. Gajek, et al., Near-field examination of perovskite-based superlenses and superlens-enhanced probe-object coupling, *Nat. Commun.* 2 (2011) 249. <https://doi.org/10.1038/ncomms1249>.
- [16] Y. Xin, J. Jiang, K. Huo, T. Hu, P.K. Chu, Bioactive SrTiO<sub>3</sub> nanotube arrays: strontium delivery platform on Ti-based osteoporotic bone implants, *ACS Nano.* 3 (2009) 3228–3234. <https://doi.org/10.1021/nn9007675>.
- [17] Y. Nakano, N. Ichinose, Oxygen adsorption and VDR effect in (Sr, Ca)TiO<sub>3-x</sub> based ceramics, *J. Mater. Res.* 5 (1990) 2910–2922. <https://doi.org/10.1557/JMR.1990.2910>.
- [18] Y.-S. Ham, J.-H. Koh, The dielectric characteristics of screen printed SrTiO<sub>3</sub>-epoxy composite thick films on the Cu plate PCB substrates, *Ferroelectrics.* 382 (2009) 85–91. <https://doi.org/10.1080/00150190902869871>.
- [19] C. Jorel, C. Vallée, P. Gonon, E. Gourvest, C. Dubarry, E. Defay, High performance metal-insulator-metal capacitor using a SrTiO<sub>3</sub>/ZrO<sub>2</sub> bilayer, *Appl. Phys. Lett.* 94 (2009) 253502. <https://doi.org/10.1063/1.3158951>.
- [20] T. Menke, R. Dittmann, P. Meuffels, K. Szot, R. Waser, Impact of the electroforming process on the device stability of epitaxial Fe-doped SrTiO<sub>3</sub> resistive switching cells, *J. Appl. Phys.* 106 (2009) 114507. <https://doi.org/10.1063/1.3267485>.
- [21] D. Merten, K.T. Kallis, H. Körner, S. Schmeinck, J. Zimmermann, H. L. Fiedler, Production of polycrystalline Bi<sub>2</sub>Te<sub>3</sub> nanostructures and the effect of annealing on their electrical conductivity, *Microelectron. Eng.* 214 (2019) 44–49. <https://doi.org/10.1016/j.mee.2019.04.023>.

- [22] J.A. Noland, Optical absorption of single-crystal strontium titanate, *Phys. Rev.* 94 (1954) 724. <https://doi.org/10.1103/PhysRev.94.724>.
- [23] R. Moos, W. Menesklo, K. Hårdtl, Hall mobility of undoped n-type conducting strontium titanate single crystals between 19 K and 1373 K, *Appl. Phys. A* 61 (1995) 389–395. <https://doi.org/10.1007/BF01540113>.
- [24] N.H. Chan, R. Sharma, D.M. Smyth, Nonstoichiometry in SrTiO<sub>3</sub>, *J. Electrochem. Soc.* 128 (1981) 1762–1769. <https://doi.org/10.1149/1.2127727>.
- [25] R. Moos, K.H. Hardtl, Defect chemistry of donor-doped and undoped strontium titanate ceramics between 1000° and 1400° C, *J. Am. Ceram. Soc.* 80 (1997) 2549–2562. <https://doi.org/10.1002/chin.199801007>.
- [26] A.F. Wells, *Structural inorganic chemistry*, Oxford University Press. (2012).
- [27] T. Klaytae, S. Thoutom, Microstructure and dielectric properties of ST ceramics prepared by the sol–gel combustion technique with chitosan addition, *Ceram. Int.* 41 (2015) S117–S122. <https://doi.org/10.1016/j.ceramint.2015.03.208>.
- [28] C.-F. Kao, W.-D. Yang, Preparation and electrical properties of fine strontium titanate powder from titanium alkoxide in a strong alkaline solution, *Mater. Sci. Eng. B* 38 (1996) 127–137. [https://doi.org/10.1016/0921-5107\(95\)01512-4](https://doi.org/10.1016/0921-5107(95)01512-4).
- [29] M.V. Raymond, V.R. Amarakoon, Microstructure and electrical properties of chemically prepared Nb<sub>2</sub>O<sub>5</sub>-doped SrTiO<sub>3</sub> ceramics, *J. Am. Ceram. Soc.* 73 (2005) 1308–1311. <https://doi.org/10.1111/j.1151-2916.1990.tb05196.x>.
- [30] R.D. Shannon, Revised effective ionic radii and systematic studies of interatomic distances in halides and chalcogenides, *Acta Crystallogr. A* 32 (1976) 751–767. <https://doi.org/10.1107/S0567739476001551>.
- [31] B. Madhavan, A. Ashok, Characterisation and dielectric property analysis of A-site doped LaTiO<sub>3</sub>-δ perovskites synthesised by ball milling method, *Adv. Matter. Lett.* 6 (2015) 395–401. <https://doi.org/10.5185/amlett.2015.5827>.
- [32] E. Echeverri, O. Arnache, Structural and impedance analysis of Co-doped SrTiO<sub>3</sub> perovskite, *J. Phys.* 687 (2016) 012040. <https://doi.org/10.1088/1742-6596/687/1/012040>.
- [33] C.B. Kaynak, M. Lukosius, B. Tillack, C. Wenger, T. Blomberg, G. Ruhl, Single SrTiO<sub>3</sub> and Al<sub>2</sub>O<sub>3</sub>/SrTiO<sub>3</sub>/Al<sub>2</sub>O<sub>3</sub> based MIM capacitors: Impact of the bottom electrode material, *Microelectron. Eng.* 88 (2011) 1521–1524. <https://doi.org/10.1016/j.mee.2011.03.022>.
- [34] Q. Khushi Muhammad, Impedance analysis and conduction mechanism of Ba doped Mn<sub>1.75</sub>Ni<sub>0.7</sub>Co<sub>0.52</sub>Cu<sub>0.05</sub>O<sub>4</sub> NTC thermistors, *Project*. (2017).
- [35] D. Hu, M. Shen, W. Cao, Dielectric enhancement in interface-modified BaTiO<sub>3</sub>/SrTiO<sub>3</sub> multilayered films prepared by pulsed laser deposition, *Microelectron. Eng.* 83 (2006) 553–556. <https://doi.org/10.1016/j.mee.2005.12.007>.
- [36] M.A. Rafiq, M.N. Rafiq, K.V. Saravanan, Dielectric and impedance spectroscopic studies of lead-free barium-calcium-zirconium-titanium oxide ceramics, *Ceram. Int.* 41 (2015) 11436–11444. <https://doi.org/10.1016/j.ceramint.2015.05.107>.
- [37] J. Suchanicz, The low-frequency dielectric relaxation Na<sub>0.5</sub>Bi<sub>0.5</sub>TiO<sub>3</sub> ceramics, *Mater. Sci. Eng. B* 55 (1998) 114–118. [https://doi.org/10.1016/S0921-5107\(98\)00188-3](https://doi.org/10.1016/S0921-5107(98)00188-3).
- [38] S. Sen, R. Choudhary, Impedance studies of Sr modified BaZr<sub>0.05</sub>Ti<sub>0.95</sub>O<sub>3</sub> ceramics, *Mater. Chem. Phys.* 87 (2004) 256–263. <https://doi.org/10.1016/j.matchemphys.2004.03.005>.
- [39] J. Xia, Q. Zhao, B. Gao, A. Chang, B. Zhang, et al., Sintering temperature and impedance analysis of Mn<sub>0.9</sub>Co<sub>1.2</sub>Ni<sub>0.27</sub>Mg<sub>0.15</sub>Al<sub>0.03</sub>Fe<sub>0.45</sub>O<sub>4</sub> NTC ceramic prepared by W/O microemulsion method, *J. Alloys Compd.* 617 (2014) 228–234. <https://doi.org/10.1016/j.jallcom.2014.07.149>.
- [40] S. Song, Z. Ling, F. Placido, Impedance analysis of MnCoCuO NTC ceramic, *Mater. Res. Bull.* 40 (2005) 1081–1093. <https://doi.org/10.1016/j.materresbull.2005.04.001>.
- [41] R. Sagar, R. Raibagkar, Complex impedance and modulus studies of cerium doped barium zirconium titanate solid solution, *J. Alloys Compd.* 549 (2013) 206–212. <https://doi.org/10.1016/j.jallcom.2012.09.062>.
- [42] C. Suman, K. Prasad, R. Choudhary, Impedance analysis of Pb<sub>2</sub>Sb<sub>3</sub>LaTi<sub>5</sub>O<sub>18</sub> ceramic, *Mater. Chem. Phys.* 97 (2006) 425–430. <https://doi.org/10.1007/BF02707284>.
- [43] A. Shukla, R.N.P. Choudhary, A.K. Thakur, D.K. Pradhan Structural, microstructural and electrical studies of La and Cu doped BaTiO<sub>3</sub> ceramics, *Phys. B: Condens. Matter* 405 (2010) 99–106. <https://doi.org/10.1016/j.physb.2009.08.075>.
- [44] S. Sen, S.K. Mishra, S.S. Palit, S.K. Das, A. Tarafdar, Impedance analysis of 0.65Pb(Mg<sub>1/3</sub>Nb<sub>2/3</sub>)O<sub>3</sub>–0.35PbTiO<sub>3</sub> ceramic, *J. Alloys Compd.* 453 (2008) 395–400. <https://doi.org/10.1016/j.jallcom.2006.11.126>.
- [45] C. Koons, On the dispersion of resistivity and dielectric constant of some semiconductors at audio frequencies, *Phys. Rev.* 83 (1951) 121. <https://doi.org/10.1103/PhysRev.83.121>.
- [46] A.K. Jonscher, The universal dielectric response, *Nature* 267 (1977) 673–679. <https://doi.org/10.1038/267673a0>.
- [47] M.A. Rafiq, Q.K. Muhammad, S. Nasir, U. Amin, A. Maqbool, Z. Ahmad, Structure, infra-red, dielectric properties and conduction mechanism of Ti and Cu–Ti co-doped bismuth ferrite (BiFeO<sub>3</sub>): a comparison study, *Appl. Phys. A*. (2018) 124. <https://doi.org/10.1007/s00339-018-2170-8>.
- [48] M.A. Rafiq, A. Tkach, M.E. Costa, P.M. Vilarinho, Defects and charge transport in Mn-doped K<sub>0.5</sub>Nb<sub>0.5</sub>NbO<sub>3</sub> ceramics, *Phys. Chem. Chem. Phys.* 17 (2015) 24403–24411. <https://doi.org/10.1039/C5CP02883C>.
- [49] J.R. Macdonald, W.B. Johnson, *Fundamentals of impedance spectroscopy. Impedance Spectroscopy: Theory, Experiment, and Applications*, Third Edition, John Wiley & Sons, Ltd. (2005) 1–26. <https://doi.org/10.1002/9781119381860.ch1>.
- [50] A. Peláiz-Barranco, J.D.S. Guerra, R. López-Noda, E.B. Araújo, Ionized oxygen vacancy-related electrical conductivity in (Pb<sub>1-x</sub>Lax)(Zr<sub>0.90</sub>Ti<sub>0.10</sub>)<sub>1-x/4</sub>O<sub>3</sub> ceramics, *J. Phys. D: Appl. Phys.* 41 (2008) 215503. <https://doi.org/10.1088/0022-3727/41/21/215503>.
- [51] J.R. MacCallum, C.A. Vincent, *Polymer electrolyte reviews*, Springer Dordrecht. (1989)
- [52] A. Kyritsis, P. Pissis, J. Grammatikakis, Dielectric relaxation spectroscopy in poly (hydroxyethyl acrylates)/water hydrogels, *J. Polym. Sci. B: Polym. Phys.* 33 (1995) 1737–1750. <https://doi.org/10.1002/polb.1995.090331205>.
- [53] V. Prakash, S. Choudhary, T. Sinha, Dielectric relaxation in complex perovskite oxide BaCo<sub>1/2</sub>W<sub>1/2</sub>O<sub>3</sub>, *Phys. B: Condens. Matter* 403 (2008) 103–108. <https://doi.org/10.1016/j.physb.2007.08.015>.
- [54] R. Tripathi, A. Kumar, C. Bharti, T.P. Sinha, Dielectric relaxation of ZnO nanostructure synthesized by soft chemical method, *Curr. Appl. Phys.* 10 (2010) 676–681. <https://doi.org/10.1016/j.cap.2009.08.015>.
- [55] J. Han, F. Wan, Z. Zhu, W. Zhang, Dielectric response of soft mode in ferroelectric SrTiO<sub>3</sub>, *Appl. Phys. Lett.* 90 (2007) 031104. <https://doi.org/10.1063/1.2431448>.
- [56] A. Pashkin, S. Kamba, M. Berta, J. Peltzel, G.D.C. Csete de Györgyfalva, et al., High frequency dielectric properties of CaTiO<sub>3</sub>-based microwave ceramics, *J. Phys. D: Appl. Phys.* 38 (2005) 741. <https://doi.org/10.1088/0022-3727/38/5/012>.
- [57] Z. Sun, Y. Pu, Z. Dong, Y. Hu, X. Liu, P. Wang, Effect of Zr<sup>4+</sup> content on the TC range and dielectric and ferroelectric properties of BaZr<sub>x</sub>Ti<sub>1-x</sub>O<sub>3</sub> ceramics prepared by microwave sintering, *Ceram. Int.* 40 (2014) 3589–3594. <https://doi.org/10.1016/j.ceramint.2013.09.069>.
- [58] O. Raymond, R. Font, N. Suárez-Almodovar, J. Portelles, J.M. Siqueiros, Frequency-temperature response of ferroelectromagnetic Pb(Fe<sub>1/2</sub>Nb<sub>1/2</sub>)O<sub>3</sub> ceramics obtained by different precursors. Part I. Structural and thermo-electrical characterization, *J. Appl. Phys.* 97 (2005) 084107. <https://doi.org/10.1063/1.1870099>.